Characterization of CVD Heavily B-Doped Diamond Thin Films for Multi Electrode Array Biosensors

"Characterization of CVD heavily B-doped diamond thin films for Multi Electrode Array biosensors"

G. Pippione, P. Olivero, M. Fisher, M. Schreck, A. Pasquarelli, Physica Status Solidi A 214 (11), 1700223 (2017)

DOI: 10.1002/pssa.201700223

Characterization of CVD heavily B-doped diamond thin films for Multi Electrode Array biosensors

G. Pippione[*1, 2], P. Olivero[1], M. Fisher[3], M. Schreck[3] and A. Pasquarelli[2]**

[1] Physics Department and "NIS" Inter-department centre, University of Torino, 10125 Torino, Italy.
[2] Institute of Electron Devices and Circuit, Ulm University, 89069 Ulm, Germany.
[3] Institut für Physik, Universität Augsburg, 86135 Augsburg, Germany.

Received ZZZ, revised ZZZ, accepted ZZZ
Published online ZZZ (Dates will be provided by the publisher.)

Keywords nanocrystalline diamond, conductivity, noise, transparency.

* giulia.pippione@gmail.com.
** Corresponding author: alberto.pasquarelli@uni-ulm.de, Phone: +49 731 5025373, Fax: +49 731 5026155

Nanocrystalline Diamond is an excellent material for the fabrication of Multi Electrode Arrays used to monitor the activity of biological cells and tissues. Yet the overall performances in terms of background noise, electrochemical activity and transparency for fluorescent detection are difficult to optimize. Aim of this study is to obtain an orientative guide on how to reach a good compromise among competing properties. To this purpose we produced, under a variety of synthesis conditions, several samples of diamond films to be employed in the fabrication of amperometric Multi Electrode Arrays.
After the fabrication, the samples were characterized from a structural, electrical, electrochemical and optical point of view in order to find possible correlations with the parameters adopted in their production.

1 Introduction

Boron-doped diamond (BDD) Multi Electrode Arrays (MEAs) are planar sensors that allow the non-invasive measurement of the secretory and bioelectrical activity of *in vitro* cell cultures, with high temporal and spatial resolution [1]. It is possible to investigate the cellular activity by measuring the action potential thanks to the capacitive coupling between the cellular membrane and the sensing electrode (potentiometry) [2-5], or the redox current due to the oxidation of neurotransmitters released during exocytotic events (amperometry) [6]. Furthermore, MEAs fabricated on transparent substrates allow simultaneous fluorescence and bioelectrical investigations, e.g. monitoring by fluorescence microscopy the intracellular calcium oscillations, which cannot be detected by electrical methods [7, 8].
The dominant noise source in measurements with microelectrodes is the thermal noise originating at the electrode electrolyte interface [12]. However, the optimization of the signal-to-noise ratio for potentiometry and amperometry goes in two different directions. In the first case, an electrode is connected to a high-impedance voltage amplifier, which measures an open circuit potential and therefore, the relevant noise parameter is the total voltage power spectral density. Under optimal conditions, this is dominated by (and proportional to) the electrochemical impedance of the electrode. Consequently, low-noise potentiometric electrodes, independently form the chosen technology, are designed for large capacity and low resistance. In most cases this goal is achieved by providing a 3D-structure of the electrode active surface, e.g. by roughening, using fractal or porous materials [9, 10]. Other authors used scaffolds of nanowires, overgrown with a biocompatible material to enhance cell viability [3, 11]. Unfortunately, all these strategies spoil the electrodes transparency so that simultaneous fluorescence measurements like confocal imaging or TIRF (total internal reflection fluorescence) are no longer possible due to the need of an inverted microscope.
In case of amperometry, the electrode is short-circuited to the virtual ground of a transimpedance amplifier and the current is measured. In this case, the relevant noise parameter is the total current power spectral density, which in turn is proportional to the real part of the admittance of the electrode [12]. Since the electrode admittance is dominated by its constant phase element (CPE), the current standard deviation results in good approximation proportional to the square root of the area of the working electrode [12]. In other words, the noise in an amperometric measurement is proportional to the electrode capacity and can be improved by reducing the electrode area, but this improvement is

possible until the amplifier noise becomes dominating [13]. This result is convenient for fluorescent measurements because a smooth planar surface combines lower capacity and lower light scattering and absorption, i.e. lower noise and better transmissivity.

If we now consider the outstanding chemical resistance and biocompatibility of diamond, which can outcompete most other materials suitable for amperometric measurements, it can be understood that in this field diamond electrodes have very high chance of becoming the material of choice, or the "gold standard". On the contrary, in the field of potentiometry, other technologies are very solidly established thanks to their excellent overall characteristics and therefore the competition for diamond as alternative material is much harder.

In light of the above considerations, the aim of this study is the characterization of boron-doped diamond films employed for the fabrication of MEAs. Here the focus is predominantly directed on amperometry, although based on the same method also an optimization for potentiometric use is possible. The tests included structural, electrical, electrochemical and optical analyses of BDD-samples, in order to identify possible correlations between their fabrication parameters, as well as to achieve a further an optimization of their performances. In particular, the background noise and the transparency appear to be in competition with each other: by rising the boron concentration the thermal noise and resistivity are reduced, while optical absorption increases and vice versa. It is therefore important to check under which conditions the efficacy of the boron-doping can be improved in order to avoid or at least minimize the amount of inactivated boron atoms, which spoil the transparency, do not contribute to conductivity and further, by acting as traps for charge carriers, can generate a significant amount of recombination/generation-noise (RG-noise).

For this analysis, fifteen nanocrystalline diamond (NCD) samples were produced by Chemical Vapor Deposition (CVD), employing hot-filament and microwave reactors. An intrinsic diamond layer was grown on three different substrate materials (glass AF32eco, Silicon wafers and single crystal diamond), onto which a heavily doped BDD layer (doping level above 10^{20} cm^{-3}) was grown. This substrate selection was based on the consideration that *i*) glass AF32eco has a coefficient of thermal expansion (CTE) nearly identical to silicon, but is subject to deformations above ~ 690 °C, *ii*) silicon withstands much higher temperatures, but is non-transparent and *iii*) single crystal diamond (SCD) is both transparent and suitable for high temperatures and leads to the growth of homoepitaxial layers. In the present context, samples grown on SCD substrates with [100] orientation can be considered as "ideal model systems". Thus, this sample collection was expected to deliver detailed evidence on the role played by the CVD parameters on the overall performances.

For the various growth runs, process parameters like substrate temperature, CH_4/H_2 ratio, boron doping method, etc. were systematically varied. The surface and structural properties of the samples were analyzed by scanning electron microscopy and Raman spectroscopy. The electrical characterization was carried out by combining Hall Effect and Van der Pauw measurements.

Cyclic voltammetry (CV) and electrochemical impedance spectroscopy (EIS) were carried out to test the electrochemical behavior of the BDD films. Each sample exhibited a potential window larger than 2.5 V, while the background current did not exhibit a clear dependence on the grain size. From EIS data, an equivalent electrical circuit was derived to model the charge transport in the electrolyte-diamond system. Lastly, by using the equivalent circuits obtained from EIS, the total noise observed during a typical experiment was modelled in terms of thermal noise from the electrolyte and from the BDD structures.

2 Sample fabrication

Fifteen samples were produced by Chemical Vapor Deposition (CVD), employing hot filament and microwave reactors [14]. Thirteen of those samples were fabricated by first growing an intrinsic nanocrystalline diamond layer on hetero substrates and after that a heavily-doped BDD layer (doping level above 10^{20} cm^{-3}) was grown. For the two single-crystal diamond samples, only the doped layer was grown. Three kinds of substrate were adopted: 25×25 mm^2 samples of glass "AF32eco" [1] with a thickness of 200 µm, 4-inch silicon wafers and single-crystal diamond with size of 10×10×1 mm^3. Each substrate was carefully cleaned by sonication in acetone and then in isopropyl alcohol for 5 minutes. This was followed by a 10 minutes treatment in "piranha" solution (H_2SO_4 and H_2O_2 in 2:1 ratio) to complete the cleaning and make the surface terminations rich in hydroxyl groups, i.e., highly hydrophilic.

The heteroepitaxial growth of diamond requires a starting layer, which, in case of non-insulating materials like silicon, can be provided by a bias nucleation process [14]. In the more general case and especially on insulating substrates, a seeding procedure can be adopted, which leaves a dense layer of diamond nanocrystals on the carrier surface. In this work, since glass is insulating, seeding with a nanodiamond (4-6 nm) suspension was used for all NCD-samples.

The relatively weak bonds formed between the seeds and the substrate may not withstand the inner stress during the following overgrowth conditions. To reinforce the adhesion, the samples were first exposed to a short CVD process (10 minutes) in a custom-made MW plasma reactor at pressure of ~1.4 kPa in a gas mix of 1.3% CH_4 in H_2 and substrate temperature of ~610 °C. The short duration of this CVD step is due to the non-homogeneous heating of the sample observed in this specific MW-reactor used for intrinsic growth, which may lead to significant deformations of the glass carrier at longer growth times. Then,

the two main CVD steps were performed to grow first a ~1 µm layer of intrinsic nanocrystalline diamond (iNCD) and then a ~300 nm BDD layer. The relatively thick undoped buffer layer was grown to prepare the diamond layer for the BDD epitaxy. In fact, it provides a background with crystallites of a few hundred nanometer, which is beneficial for the carrier mobility and at the same time reduces the density of defects (grain boundaries). These defects act as parasitic recombination-generation (RG) centers and have a negative influence on the noise performance of the grown material. For all glass and silicon samples, except samples AF92 and AF93, the iNCD layer was grown in a Hot Filament reactor at a chamber pressure of 2 kPa, ramping-up the power for 40 minutes, until reaching a filament temperature of 2100 °C and then keeping the process parameters constant for 20 hours.

The glass substrate temperature was kept below 650 °C and the gas flux included 1.6 sccm CH_4 and 400 sccm H_2. The uniformity of the temperature distribution in the HF-reactor is much better than in the MW-reactor and even after 20 hours at 650 °C, the glass deformations are negligible.

The silicon substrate temperature was retained at ~750 °C for both iNCD and BDD depositions, while the growth (BDD-only) on the two single crystal diamond substrates were performed at 615 °C and 750 °C respectively.

The boron-doped growth was performed in a dedicated Microwave reactor (Astex AX3120). The MW power was in the 750 - 1200 W range, the hydrogen and methane fluxes were set at 200 sccm and 3 sccm respectively, and the process pressure was 30 Torr. Boron wires were inserted into the plasma as solid source for boron-doping, by means of a magnetic slider. The doping level could be adjusted by varying the insertion length of the wires in the plasma (approx. 6 - 7 cm) and by using one or two wires simultaneously. Every 10-12 minutes the boron source was manually pushed forward by 8 mm to expose new material within the plasma ball. For samples AF73 and AF74 the boron-doping was instead achieved with an 8 cm wide boron ring (same material of the wire) positioned around the plasma ball; in contrast to the previous method, this doping approach involves the same portion of the doping source for the entire process. For samples AF92 and AF93, both the intrinsic and the B-doped growth processes were performed in the Microwave reactor. For the first sample (AF92), the growth parameters were set in order to emulate the analogous process occurring in the Hot Filament reactor, i.e. with a gas flux of 0.8 sccm CH_4 and 200 sccm H_2, and a total growth time of 20 hours. For sample AF93 the gas flux was identical to the value for the growth of the doped material, i.e. 3 sccm CH_4 and 200 sccm H_2, for a total growth time of ~3 hours. At the end of the processes, all samples were treated for two hours in chromosulphuric acid at 100 °C, to remove the residual sp^2 phase and turn the pristine H-terminated hydrophobic surface to an oxygen-terminated, hydrophilic one. Table 1 summarizes all process parameters.

Table 1 - CVD growth parameters in Microwave Reactor. Where no specified, intrinsic growth took place in Hot-Filament reactor. Here an i-prefix corresponds to intrinsic growth, and b-prefix to boron-doped growth.

Sample ID	Material	MW power (W)	Press (Torr)	H_2 flow (sccm)	CH_4 flow (sccm)	T-sample (°C)	Boron rods (# x cm)	Growth time (min)
AF72	AF32eco	900	30	200	3	635	2 x 7	b60
AF73	AF32eco	600	30	200	3	635	ring 8 cm	b60
AF74	AF32eco	750	30	200	3	650	ring 8 cm	b60
AF75	AF32eco	900	30	200	3	630	1 x 14	b60
AF82	AF32eco	1000	30	200	3	630	2 x 6.5	b60
AF83	AF32eco	900	30	200	3	630	2 x 6.5	b60
AF84	AF32eco	900	30	200	3	620	2 x 6.5	b60
AF85	AF32eco	900	30	200	3	620	2 x 6.5	b60
AF86	AF32eco	900	30	200	3	615	2 x 6.5	b60
AF93	AF32eco	900	30	200	3	615	2 x 6.5	i200-b60
AF92	AF32eco	i750-b900	30	200	i0,8-b3	i560-b615	2 x 6.5	i1200-b60
Si03	Si+SiO_2	1200	40	200	1,5	750	2 x 6.5	i40+b60
Si04	Si+SiO_2	1200	40	200	2	750	2 x 6.5	i40+b45
AS01	SCD [100]	900	30	200	3	615	2 x 6.5	b60

AS02	SCD [100]	900	30	200	3	750	2 x 6.5	b60

3 Results

3.1 Morphological characterization

After the CVD growth processes, the samples consisted of a substrate covered with an intrinsic NCD layer (~1 µm thick) and a BDD layer on the top (~300 nm thick). Thicknesses were measured by Scanning Electron Microscopy (SEM) inspection of the cross-section after dicing the samples, as very last step after all other characterizations. Very small thickness variation was observed from sample to sample, indicating little dependency of the growth-rate from temperature in the given range, since the process parameters were previously adjusted to achieve a good thickness control.

After growth, the surface morphology of the boron-doped layer was inspected by means of SEM (Fig. 1). For each sample, three micrographs were considered and the smallest and the biggest grain were measured. An average grain size was calculated and then used for comparison. Films on glass substrates exhibited an average grain size ranging between 400 nm and 500 nm, while films on silicon substrate presented a larger average gain size of ~800 nm.

The main differences between the two types of samples were substrate temperature, pressure and CH_4 concentration during the CVD processes; it is well known that these parameters influence the film morphology. At higher CH_4 concentration and pressure the growth-rate increases and at higher temperature the grains have a higher probability to grow larger before a new grain is formed [15]. Further, renucleation and formation of twins are strongly influenced by the α–parameter [16, 17], which is determined by CH_4 concentration and temperature. On the contrary, a significant temperature dependency of the growth-rate in the given temperature range was not observed, as mentioned before.

3.2 Electrical characterization

Firstly, all samples grown in the HFCVD reactor were tested after deposition of the i-NCD-layer, showing in all cases a resistivity above 10^{12} Ω cm, i.e. beyond the measurement range of the employed instrumentation. For the samples AF92, AF93, Si03 and Si04 this measurement was not possible because the BDD layer was grown seamlessly onto the i-NCD layer, i.e. without taking the samples out of the reactor. Based on previous experiences, we can realistically assume for those samples a "background" boron density in the 10^{15} cm^{-3} range. Therefore, considering a Boron activation energy of 0,37 eV, an equivalent density of states in the valence band $N_v = 10^{19}$ cm^{-3} at room temperature and a "best case" mobility, i.e. as reported for epitaxial layers of 700 cm^2/Vs [18], the resistivity is expected to be larger than 100 Ω cm. Therefore, the sheet-resistance of 1µm thick samples is expected to be larger than 1 MΩ/□. Still, the mobility in NCD is significantly lower and therefore both above-mentioned values should actually be much larger.

The electrical characterization of the BDD layers was carried out by combining Hall Effect and Van der Pauw measurements. From three measurements for every sample, the mean values and the standard deviations of carrier concentration, conductivity, mobility, resistivity and sheet resistance were calculated. The positive sign of the detected Hall coefficients confirmed that in the B-doped NCD films the conductivity is due to holes. This suggests that electronic transport due to sp^2 amorphous carbon phase in the grain boundaries (for which electron transport with a negative Hall coefficient is expected) does not play a significant role in these samples. The carrier concentration resulted in a range between 3.2×10^{20} and 3×10^{21} cm^{-3}, thus all samples are above the Mott transition (occurring at ~2×10^{20} cm^{-3} [19]) and show quasi-metallic transport behavior.

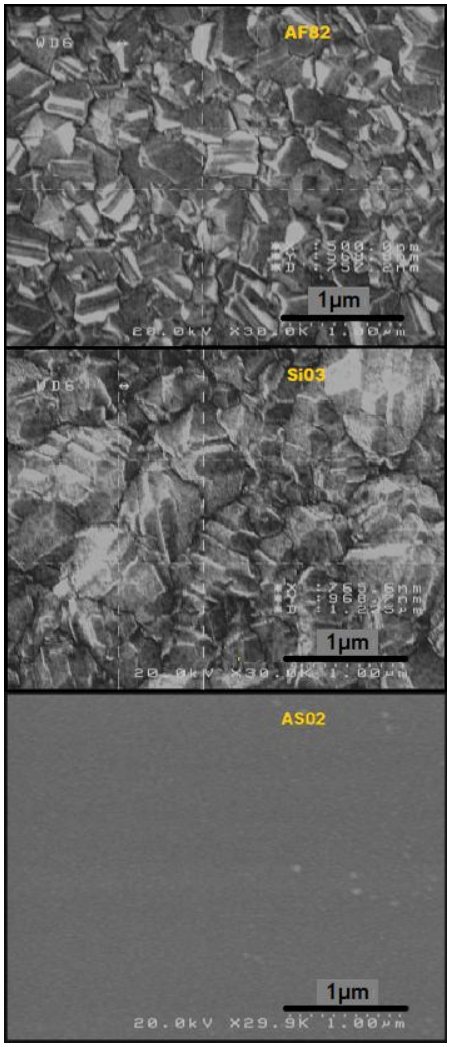

Figure 1 SEM images of BDD samples, (top) AF82 grown on a glass substrate at a temperature of ~630 °C, (center) Si03 on a silicon wafer at ~750 °C and (bottom) AS02 on SCD at ~750 °C. The polycrystalline structure of AF82 is characterized by grains with an average mean size of ~500 nm, for Si03 the grain size is ~800 nm, while on the SCD surface only small dust particles (useful for focusing) can be recognized.

The thickness is nearly the same for all samples, therefore it is equivalent to analyze the data on the basis of the sheet-resistance or the resistivity. Actually only the first one was experimentally obtained from Van der Pauw measurements and the second one, which is probably more familiar to most readers, was simply calculated dividing the sheet-resistance by the thickness. The sheet resistance ranged between

30 Ω/□ and 1.8×10^3 Ω/□, and so the conductivity resulted between 20 Ω^{-1} cm^{-1} and 1.3×10^3 Ω^{-1} cm^{-1}. The order of magnitude of the mobility was 10^{-1} cm^2 $V^{-1}s^{-1}$ for all NCD samples, except for sample AF92 for which a value of 1.14 $cm^2V^{-1}s^{-1}$ was obtained. These values are in agreement with the results of previous characterizations of CVD-grown boron-doped PCD samples reported in [20]. Fig. 2 shows sheet resistance data as a function of bulk carrier concentration. As the carrier density increases, the sheet resistance decreases. This is in qualitative agreement with the formula for the resistivity given by

$$\rho = \frac{1}{q\,p\,\mu_h} \qquad (1)$$

where q is the elementary charge, p the hole concentration and μ_h the hole mobility.

For bulk concentrations around 10^{21} cm^{-3} and above, the log-log plot shows with good approximation a linear trend with negative slope, which means that the mobility is fairly constant. Below $3x10^{21}$ cm^{-3}, formation of boron pairs or even clusters was negligible. The two samples AF73 and AF75 however fall slightly below the general trend. A reason for this could be the higher mobility observed at lower doping density due to diminished Coulomb scattering. A similar result was expected also from sample AF74, but unfortunately this sample was broken and no longer suitable for a Van der Pauw measurement. Yet, out of the largest fragment, it was still possible to analyze the electrochemical behavior and the film transparency.

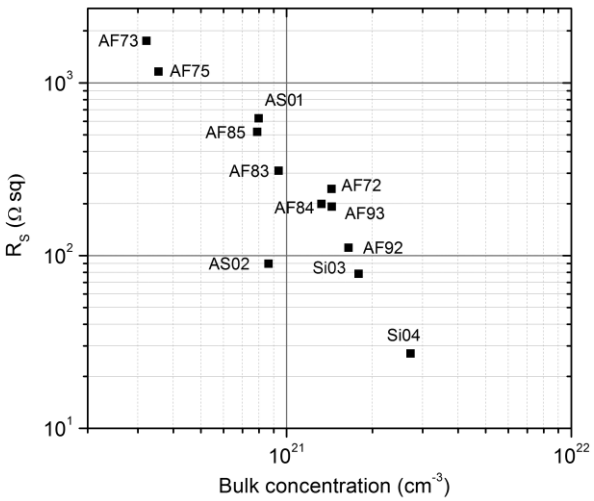

Figure 2 Sheet resistance Vs. bulk carrier concentration from combined Van der Pauw and Hall-Effect measurements.

As for the dependence of the doping efficiency on the growth temperature during CVD, Fig.3 shows the estimated values of the bulk carrier concentration as a function of the growth temperature. At high doping values (i.e. above Mott transition), boron activation at room temperature can be considered complete and thus, in first approximation, the carrier concentration can be assumed equal to the substitutional boron concentration, i.e. $p = N_a$. The data in Fig. 3 indicate a correlation between doping density and growth temperature for NCD films. We observe that for samples grown on silicon substrates (for which the growth temperature was higher by about 120 °C than for glass substrates), the carrier concentration is higher (up to 3×10^{21} cm^{-3})

while for samples on glass, all p values are comprised between 3×10^{20} and 2×10^{21} cm^{-3}. Referring to Fig. 3, data within the red ellipse refer to samples for which the doping was performed with two movable boron wires inserted into the plasma. Splitting this cluster in two subgroups and taking the mean-value of each one, it can be seen that the average bulk concentration increases as the temperature increases. Fluctuations on bulk carrier concentration may arise from other possible factors during the growth, which are not yet fully under control. For example, the previous growth process that took place in the CVD-reactor might leave a "memory" inside the reactor chamber, which leads to different starting conditions for the following process. Other reasons for this variability include the manual control of temperature and boron supply during growth.

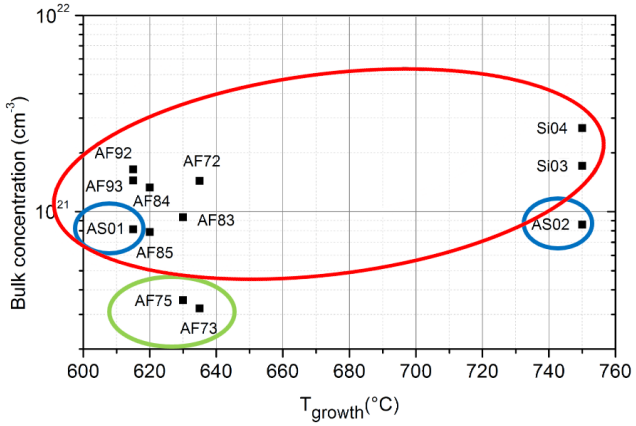

Figure 3 Bulk carrier concentration from Hall measurements versus growth temperature.

The data marked in green are AF73 and AF75. For the first sample, the doping was achieved with a boron-wire ring exposing the same area during the entire process and resulting in a "static" doping process. For AF75 only one static long boron wire was used. In both cases, the efficiency of the doping process was not optimal.

The samples grown on single-crystal diamond (marked in blue) do not show a difference in the doping level, even though they were grown at different temperatures. In these cases, the difference in conductivity can only be attributed to different mobility. This latter result suggests that at lower temperature there is a higher probability of forming defects in the crystal structure.

3.3 Electrochemical characterization

Further investigations of the boron-doped layers were carried out with the electrochemical impedance spectroscopy (EIS) and cyclic voltammetry (CV) techniques. EIS investigates the total impedance of an electrolyte-electrode system. The arrangement of the ions on the electrode surface can be represented with the Helmholtz double layer model, while, due to the equilibration of the Fermi levels of the two different phases, the resulting band bending defines a space charge layer within the semiconductor (Fig. 4b). In the specific case of an electrolyte-BDD system, the equivalent total impedance can be modeled as usually done for a polarizable semiconductor electrode [21-23]. In Fig. 4a the resistor R_s represents the bulk resistance of the BDD layer, which cannot be neglected in case of a semiconductor, while R_{SC} and Q_{SC} represent respectively a leakage current path and the capacity of the depleted space charge layer in the BDD layer (Q_{SC} is a constant phase element CPE, which models a non-ideal capacitor). The double layer can be represented as a Randle cell, i.e. an RQ circuit with double layer capacitance Q_{DL} (a CPE) and double layer resistance R_{DL}, which is a representation of the activity occurring on the surface. R_{sol} is the ohmic resistance of the electrolyte. For clarity, R_s and R_{sol} are shown in Fig. 4a as separated elements because of their different physical nature, but since they result connected in series, only their sum can be obtained by EIS. The impedance spectroscopy was performed in a three-electrode cell, making use of an Ag/AgCl reference electrode and a 100 mm^2 Pt counter electrode. The square BDD film was contacted by silver paint along the four borders with the underlying copper plate carrier and then this electrode structure was encapsulated in adhesive Teflon films with a hole of 1 mm^2 providing the interface between the BDD sample and the electrolyte (0.1 M KCl). An AC voltage of 10 mV_{rms} amplitude was applied between the working and the counter electrode. From the current measured at the working electrode, the phase shift and amplitude of the complex impedance was obtained in a frequency range varying from 0.1 Hz to 1 MHz. The amplitude of the complex impedance and the phase shift were plotted versus frequency to produce a Bode plot. An example of EIS data is shown in Fig. 5 for sample AF84. The Bode plot shows the typical behavior of polarizable electrodes, as one would expect from BDD, with a dominant capacitive component at low frequencies and a dominant resistive component at high frequencies. Experimental data were then fitted with equation (2), which describes the complex impedance of the system shown in Fig.4b as a function of frequency, interpreted with a charge-transfer process dominated by two time constants.

Fit parameters are reported in Tab. 2. R_s+R_{sol} is the sum of semiconductor and solution resistances. However, given the conductivity of 13 mS/cm for a 0.1 M KCl solution at 25°C, and considering the area of the working and counter electrodes as well as a distance between the two of 1 cm, R_s is expected to be dominating with respect to R_{sol}. From Eq. 2 the power value n_{dl} is in the 0.76 - 0.95 range, thus confirming the applicability of the adopted model. Instead n_{sc} is very close or equal to 1, in other words the space charge layer behaves like an ideal capacitor. The circuit shown in Fig.4a represents therefore a satisfactory model for all samples.

The validity of this model was further checked with noise spectroscopy measurements and modelling, as described below. In this analysis, the noise arising from the electrical

circuit reported in Fig.4a was first simulated, making use of the fitted parameters previously obtained from the EIS, and then compared with the experimental noise spectra measured with the real samples.

(2)

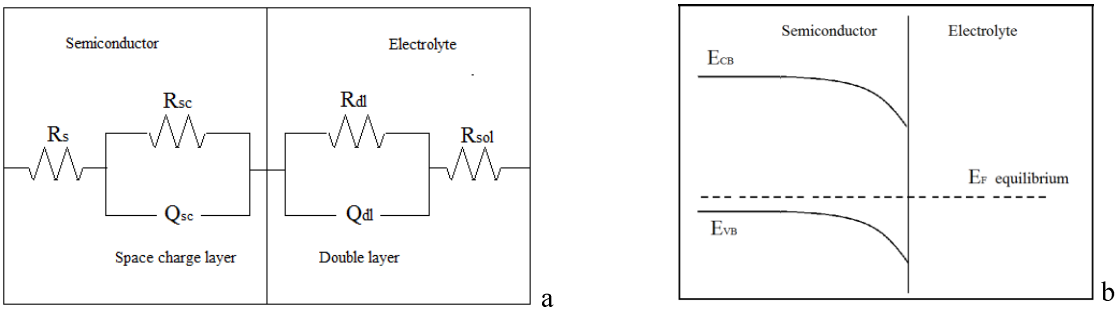

Figure 4 a) Equivalent electrical circuit for the polarizable diamond/electrolyte interface. The right part of the circuit includes a resistive element associated to the solution, a double layer capacity Q_{dl} placed in parallel to the faradaic impedance R_{dl} associated to the activity on the surface. The left part of the circuit includes a parallel of the resistor R_{sc}, representing a leakage current path through the space charge layer, and an impedance Q_{sc} that represents the space charge layer capacitor. b) The space charge layer in diamond is caused by the band bending induced by the oxygen termination [24], which depletes holes. Lastly, R_s is the ohmic resistance of the boron-doped layer. Both capacities Q_{sc} and Q_{dl} are modeled for the fit as CPE with exponents n_{sc} and n_{dl} respectively.

Table 2 EIS data fitted with Eq. 2. Fit parameters refer to the equivalent electrical circuit shown in Fig 4a.

Sample	R_s+R_{sol} (Ω)	Q_{dl} (F)	n_{dl}	R_{dl} (Ω)	Q_{sc} (F)	n_{sc}	R_{sc} (Ω)	X^2_{red}
AF74	1.06×10^{4}	2.51×10^{-7}	0.87	1.72×10^{6}	8.67×10^{-8}	1.00	5.74×10^{7}	0.090
AF82	7.18×10^{3}	9.52×10^{-7}	0.86	2.22×10^{7}	2.12×10^{-7}	0.95	9.24×10^{4}	0.041
AF83	1.29×10^{4}	7.3×10^{-7}	0.86	1.10×10^{5}	2.17×10^{-7}	1.00	5.72×10^{7}	0.020
AF84	5.53×10^{3}	3.12×10^{-7}	0.92	3.59×10^{7}	3.54×10^{-7}	0.96	6.95×10^{4}	0.034
AF85	7.57×10^{3}	2.81×10^{-7}	0.89	1.77×10^{8}	4.45×10^{-7}	0.94	9.20×10^{4}	0.043
AF86	5.49×10^{3}	1.79×10^{-6}	0.95	9.01×10^{6}	2.01×10^{-7}	0.95	5.79×10^{4}	0.041
AF92	5.92×10^{3}	3.46×10^{-7}	0.93	1.82×10^{6}	1.64×10^{-7}	0.98	3.26×10^{7}	0.040
AF93	5.40×10^{3}	2.76×10^{-7}	0.90	3.62×10^{5}	3.64×10^{-7}	1.00	1.79×10^{6}	0.034
Si03	5.19×10^{3}	8.39×10^{-7}	0.90	2.01×10^{5}	8.84×10^{-7}	0.93	1.57×10^{5}	0.039
Si04	5.7×10^{3}	2.57×10^{-6}	0.89	5.62×10^{6}	1.84×10^{-7}	0.96	1.88×10^{5}	0.044
AS01	6.42×10^{3}	1.33×10^{-7}	0.97	2.16×10^{7}	1.92×10^{-8}	1.00	6.61×10^{7}	0.041
AS02	5.25×10^{3}	2.91×10^{-7}	0.98	5.12×10^{7}	4.14×10^{-8}	1.00	8.23×10^{7}	0.038

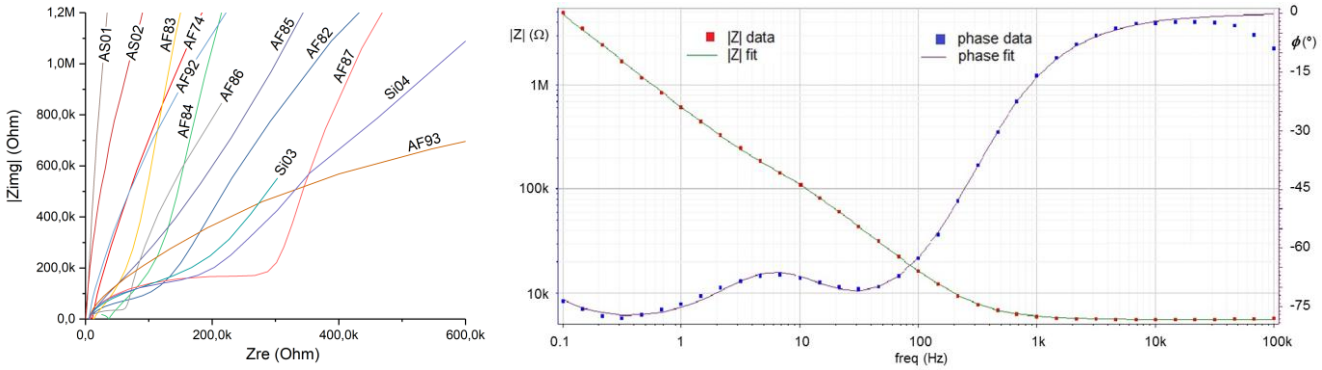

Figure 5 (Left) Nyquist plots of all measured EIS data. (Right) Bode plot of experimental EIS data and fit curves for sample AF84.

In details, the noise was measured with the same three-electrode electrochemical cell previously used for EIS measurements, using the BDD samples as electrodes. The current noise signal coming from the BDD electrode was conditioned by a transimpedance amplifier, with a choice of 100 MΩ or 1 GΩ as feedback resistor, followed by a low-pass filter and finally connected with a data-acquisition unit. The amplifiers used in the front-end stage are FET-input, very low-bias, low-noise "AD8626" from Analog Devices. Next, the signals are low-pass filtered (3 dB at 1 kHz) with a 4th-order Bessel topology and connected by means of differential lines to a National Instruments USB-6216 data-acquisition unit, working at a sampling rate of 4 kHz. Note that this is the same acquisition circuit employed during biological experiments. Fig. 6a, shows as an example the noise spectrum measured with sample AF84. Using LTspice software from Linear Technology (the complete circuit is depicted in Fig.7), we simulated not only the overall noise performance, but it was also possible to break-down the total system noise in order to separately obtain the noise of the electronic signal-conditioning chain and the noise contributions from each element of the equivalent circuit of the electrolyte/electrode system. By comparing the simulated and experimental spectra, we note that they are very similar; both spectra present in the working bandwidth the typical shape of a derivator, followed by the low-pass filter cut-off. These results confirm again the consistency of the EIS equivalent circuit and additionally confirm the conclusions obtained from the impedance spectroscopy, regarding the charge transfer model. Furthermore, this analysis suggests that the noise is predictable in terms of thermal noise generated at the electrode/electrolyte interface, and therefore these contributions can be minimized only to a limited extent. Table 3 shows a compact summary of the noise level from NCD samples.

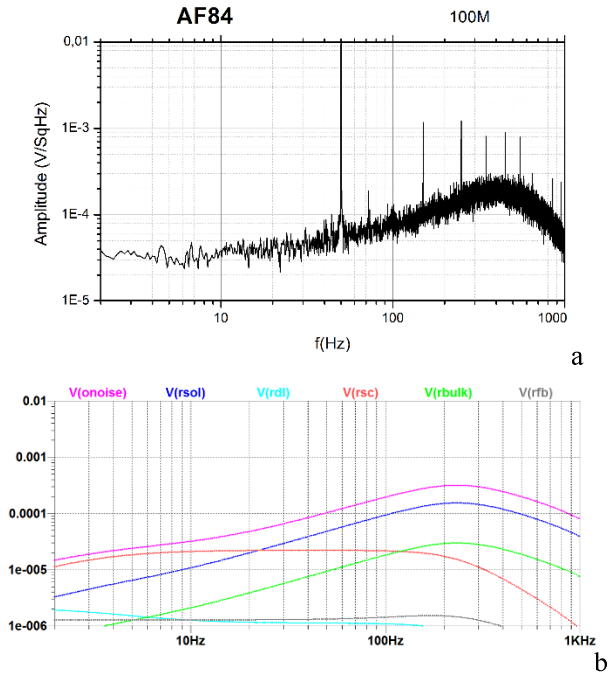

Figure 6 a) Noise spectrum recorded from sample AF84. The quasi-reference Ag/AgCl electrode is grounded. In this case the feedback resistance of the transimpedance amplifier is 100MΩ.
b) Simulated spectra obtained by using the circuit values derived from EIS (Table 2). The traces refer to thermal noise contribution of each resistor in the EIS equivalent circuit (blue R_{sol}, cyan R_{dl}, green R_{bulk}, red R_{sc}, gray for $R_{feedback}$). The magenta trace is the sum of all spectra, i.e. the overall system noise.

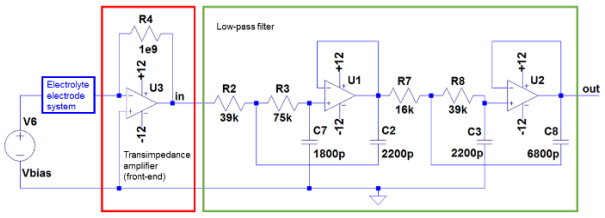

Figure 7 Schematics of the amperometric set up: the signal coming from the electrolyte/electrode system (blue box) is amplified by a transimpedance amplifier (red box). Next, the signal is low-pass filtered by a 4th-order Bessel topology (green box) and then the output is sent to the acquisition unit (not shown).

Table 3 Comparison of the noise spectral density at 100 Hz

Sample ID	e_n (V/sqrt(Hz))
AF82	6×10^{-5}
AF83	1.5×10^{-4}
AF84	8×10^{-5}
AF85	9×10^{-5}
AF86	4×10^{-5}
AF92	1.1×10^{-4}
AF93	9×10^{-5}
AS01	2.3×10^{-5}
AS02	1.8×10^{-5}
Si03	2.5×10^{-4}
Si04	1.5×10^{-4}

The electrode activity was then characterized by Cyclic Voltammetry (CV). As already mentioned, a BDD electrode is polarizable, therefore in absence of redox reactions the current through the electrode/electrolyte interface is negligible within a voltage range in which water electrolysis does not occur. This range is called *potential window* and its width is defined by the onsets of hydrogen and oxygen evolutions, in the cathodic and anodic regimes respectively, resulting from water dissociation. The background current within the potential window can be defined as [15]:

— (3)

where the capacitive charging current —is proportional to the voltage scan-rate and the total electrode/electrolyte capacitance, while the resistive (ohmic) current component is due to the parasitic chemical activity of defects (leakage resistances in the EIS) or even to physical adsorption/desorption of species present in the electrolyte. CV data were acquired using the same three-electrodes cell and electrolyte already used for EIS and noise measurements. In this case, the active area of the working electrode (BDD film) in contact with the electrolyte was 5 mm^2. A triangular voltage waveform spanning between -2 V and +2 V with a scan rate of 50 mVs^{-1}, was applied at the counter electrode and monitored through the reference electrode. The working electrode was connected to the virtual ground of the front-end transimpedance amplifier and the current flowing between counter and working electrodes was recorded. Fig. 8 shows three cycles recorded from sample AF74 at a scan rate of 50 mV/s; here we can estimate a potential window of approximately -1 – 1.5 V and a background current lower than 0.2 µA. Before the current branches due to OH- oxidation (anodic) or H+ reduction (cathodic), we can see bulges, occurring at ~1.2 V and ~ -0.7 V respectively, caused by the adsorption of such ions on the electrode surface.

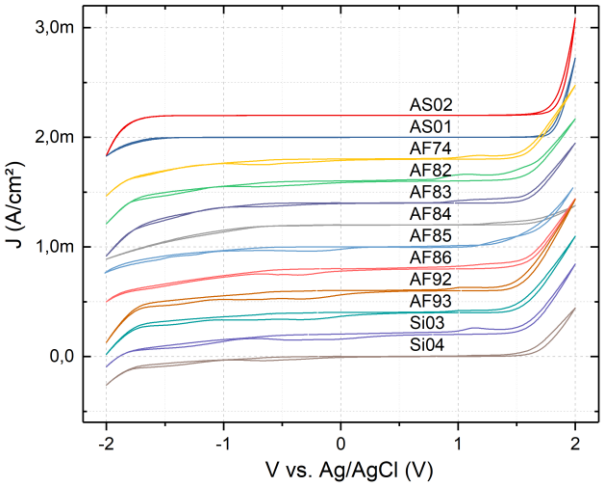

Figure 8 CV-plots at performed at a scan rate of 50 mV/s in 0.1 M KCl. For NCD samples the observable potential window is approx. -1 V – 1.5 V and for SDC samples +/- 1.5V.

By comparing the background current of every sample, it can be expected that both potential window and background current can vary according to the diamond surface quality [25]. For example, in polycrystalline and nanocrystalline diamond, the differences in the voltammograms stem from the different densities of surface defects and amount of non-diamond carbon phases, like graphite or amorphous carbon, especially at the grain boundaries. Therefore, differences in background current are possibly dependent on the grain size of surface diamond grains. For a better evaluation, we reproduced for each sample the background current of the second cycle, in Fig. 9 using a semi-logarithmic scale within a narrower region of the anodic range (0 V – 1 V). However, we can observe that all currents in the considered range are below 10 µA and the differences among them are smaller than one order of magnitude.

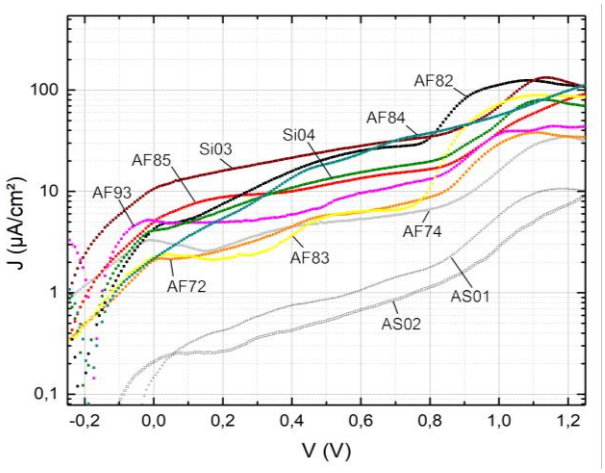

Figure 9 Background current density in logarithmic scale within the anodic part of the potential widow. For every CV curve, the anodic range of the second cycle was considered. A negligible difference in the background current is observed be-

tween films with larger grain size (~800 nm for Si03 and Si04) and films with smaller grain size (between 200 nm and 500 nm), while for the monocrystalline samples it is one order of magnitude lower.

3.4 Raman spectroscopy

Micro-Raman measurements were performed for each sample with a Horiba Jobin Yvon HR800 spectrometer interfaced with an Olympus BX41 confocal optical microscope. The spectrometer was equipped with a 1800 lines/mm grating yielding a ~2 cm^{-1} spectral resolution, and an air-cooled CCD detector. The use of a 100× magnification objective allowed for a ~2 μm beam spot. The excitation source was an Nd solid-state laser with $\lambda = 532$ nm emission wavelength and an output power of 100 mW. For each measurement, the laser beam was focused to a random point of the sample surface. The integration time for each spectrum was 1 s and each spectrum resulted from the average of 5 individual spectra. For each sample, three acquisitions from different points of the surface were performed for sake of statistical significance. We can distinguish between peaks commonly observed in polycrystalline diamond and peaks (or bands) specifically associated to the boron inclusion. The presence of non-diamond phases leads to the appearance of several peaks in the spectrum, as well as to a broadened G peak shifted between 1480 cm^{-1} and 1680 cm^{-1}.

In each spectrum, the first-order Stokes peak related to the diamond phase is well defined at a Raman-shift between 1332 cm^{-1} and 1338 cm^{-1}. This peak arises from the underlying undoped diamond layer, which is compatible with the estimated probing depth of the Raman technique.

Complementarily, the presence of amorphous carbon phase is detectable and we assume that this phase is localized at the boundaries of the diamond crystal grains. In most spectra (Figure 10a) we observed a peak between 1130 cm^{-1} and 1160 cm^{-1}, which is indicative of the presence of trans-polyacetylene at grain boundaries and interfaces [26]. Boron doping is detected from a wide band at ~1220 cm^{-1} and a peak at ~1320 cm^{-1}.

The band centered at 1220 cm^{-1} is likely to be caused by the effect of boron incorporation in the diamond lattice [27], and its appearance in the spectrum is independent from the presence of the sp^2 carbon phase in the films [27]. As the boron concentration increases, the intensity of the band at 1220 cm^{-1} increases as well, with respect to the first-order diamond line (1332 cm^{-1}).

The first order peak of diamond of the highly boron doped layer appears like a shoulder at a Raman shift between 1320 cm^{-1} and 1330 cm^{-1}. For samples AF73, AF74, AF85, AF92 and Si03, this shoulder overlaps the first-order diamond peak arising from the underlying undoped layer, while in the other cases, two distinct features are detectable.

The two above-mentioned Raman features (i.e. the first-order line from the underlying diamond layer and the boron-related peak at 1320-1330 cm^{-1}) could be conveniently interpolated with a Lorenzian peak and a Breit-Wigner-Fano function (BWF), respectively. An example is provided in Fig 10b, although it is worth remarking that at this stage it was not possible to extrapolate unequivocal correlations of the results of the fitting procedures with the estimated boron concentrations. This is most likely to be attributed to limited reproducibility of the laser focusing conditions in the measurements from different samples.

The asymmetry of diamond peak in polycrystalline BDD is typically attributed to a Fano resonance induced by the quantum mechanical interference between the discrete phonon state and the electronic continuum [27 - 29]. In an alternative interpretation, dopant incorporation at substitutional or interstitial sites can produce lattice stress that generally depends on the doping level [30]. Such stress induces a splitting of the first-order diamond line.

Regarding the SCD samples, the most important observation is the remarkable difference in the intensity of the diamond and non-diamond peaks, which indicates the effect of the temperature during the respective growth processes with respect to a possible formation of defects and the consequent formation of non-diamond phase around them.

3.5 Optical characterization

To allow the simultaneous detection of fluorescence emission and electrochemical recording, the whole device was made of transparent material, including the active diamond electrode, diamond conducting leads, diamond insulation layer and substrate. In this multilayer structure, each layer and interface contributes to a partial loss of the incident light. The optical spectral transmittance was performed in the wavelength range from 200 nm to 800 nm. Fig. 11 shows the results for all samples with BDD layer deposited on transparent substrates. Three red lines mark wavelengths commonly used in fluorescence microscopy. Samples AF92 and AS01 are clearly unsuitable for fluorescence measurements, while for suitable samples the detected transmittance ranges between 32% and 45% at wavelength of 500 nm, while at 340 nm it falls in all cases below ~35%.

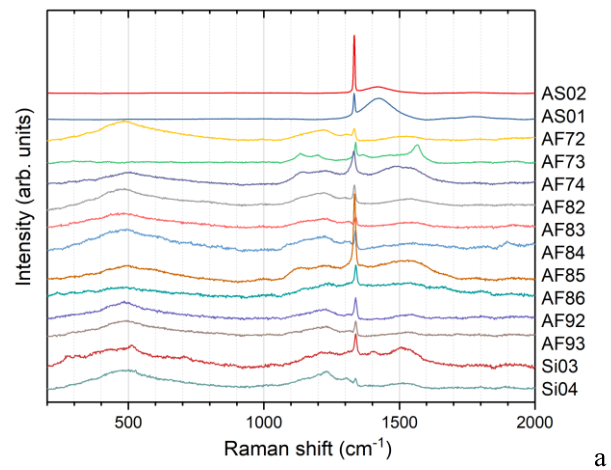

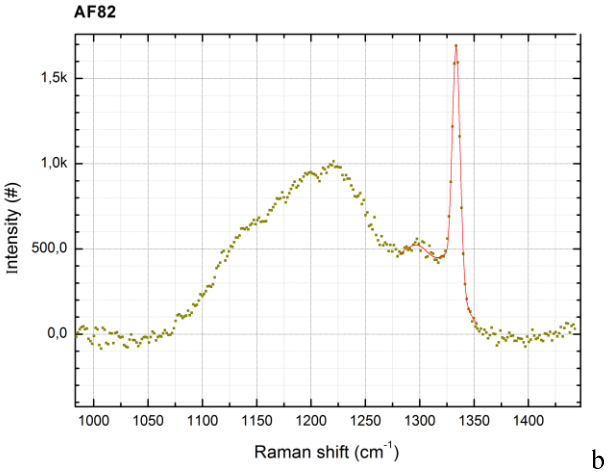

Figure 10 a) Raman spectra. b) Multiple peak fit of the first order diamond peaks related to the doped and the undoped layer of sample AF82. The used functions are respectively a BWF and a Lorentian.

In order to obtain a higher transparency, BDD layers need to be as thin as possible, while the doping concentration should be carefully optimized, to guarantee both the metallic conductivity and a low absorption coefficient [7, 20]. The two SCD samples differ substantially in this test. A first evidence is that their transparency is not better than the one measured on the NCD-samples and this can be attributed to the 1 mm thickness of the substrate. In average, the transmittance of AS02 is comparable with the medium-high range of the NCD-samples, while AS01 presents a remarkably lower transparency, nearly proportional to the wavelength.

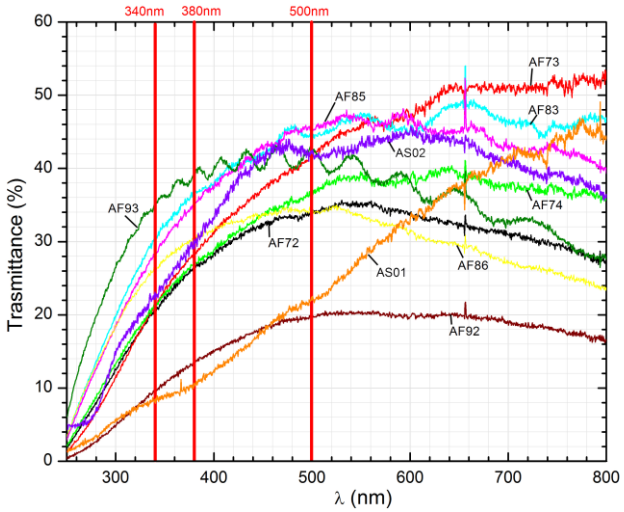

Figure 11 Transmittance spectra of all thin films on glass substrate and single crystals.

4 Discussion

The SEM morphological characterization highlighted that the growth processes at higher substrate temperatures led to a larger grain size of polycrystalline diamond. Two samples grown at different temperatures on SCD substrates were considered as "ideal model systems".

The electrical characterization, carried out by coupling Hall Effect and Van der Pauw sheet-resistance measurements, reported that the sheet-resistance decreases as the incorporation of boron during the growth process increases, and no significant correlations emerge between mobility and other possible affecting parameters (grain size, ionized acceptor, etc.). Furthermore, considering the samples characterized by the same boron doping method, a systematic dependence of the carrier concentration from the growth temperature was observed, with the exclusion of the samples grown on SCD substrate. However, in these two cases the mobility resulted significantly different. This latter finding suggests that a higher substrate temperature significantly reduces the defect formation during the CVD growth and furthermore can slightly increase the doping efficiency in nano- and poly-crystalline diamond.

From the impedance spectroscopy, an equivalent electrical circuit was derived for each sample to model the electrolyte-diamond system. With these models, we could prove that the noise detected during a typical amperometric experiment is predictable in terms of thermal noise coming from the electrolyte and from the boron-doped diamond layer. The profile of the noise spectrum is typical of a derivator and can be predicted on the basis of the equivalent electrical circuit that models the electrode/electrolyte system. The SCD samples showed, as expected, the lowest noise level, due to the virtual absence of grain boundaries responsible for RG-noise, however the best NCD sample exhibited a noise about two times larger than that of monocrystalline samples.

Subsequently, cyclic voltammetry was employed to investigate the electrochemical activity of BDD surfaces and each sample exhibited a potential window of ~ 2.5 V, while the background current did not exhibit a clear dependence from the grain size.

Raman spectroscopy was employed to analyze the structural properties of the different samples, leading to the identification of the typical diamond features within the nanocrystals and the presence of non-diamond C-phase localized along the grain boundaries. Furthermore, features due to the boron incorporation in diamond lattice were clearly observed.

Finally, optical characterization was performed on all samples grown on glass substrates and both SCD samples. In this analysis the SCD samples provided a striking evidence on the role played by the temperature in obtaining a good optical transmissivity. This result combined with the observed drop of mobility, suggests that a CVD growth process run at moderate temperature on an SCD substrate can lead to the formation of a significant amount of defects, and therefore it is plausible to speculate on the formation of some amount of sp^2 at the edges of the defects, to be responsible for the drop of transmissivity. Raman spectra of the SCD samples are consistent with this hypothesis and further evidence is provided by the electrochemical leakage current found for AS01, which was nearly two times larger than in the case of AS02.

As for the correlation of electronic noise and optical transparency, it appears that sample AF93 indicates a good overall strategy. This sample is the best one in terms of light transmission in the spectral range of interest and possesses a good noise level, indicating that a thinner i-NCD layer seamlessly overgrown with the BDD layer yields both good optical and electrical properties. A possible explanation of this remarkable result could be found in the long time available, during the intrinsic growth step, to desorb the species unavoidably introduced in the reactor chamber when loading the sample, i.e. nitrogen, oxygen and water, which may partially compensate or inactivate Boron. By comparing the results of AF93 and AF92, both seamlessly grown, it appears also evident that even a small increase in temperature from 615 to 630 °C leads to a more efficient incorporation of boron. Nevertheless, the thicker intrinsic layer of AF92, grown for 20 hours at a temperature of only 560°C spoils the transparency and degrades slightly the noise level.

Although MEAs, as the name says, consist of microelectrodes, in this study the analysis was done on macroscopic samples, i.e. unstructured films. Here the idea was to perform a classification of the raw-material at an early stage, i.e. before starting a microfabrication process. In order to predict with a good degree of confidence the behaviour and performances of microelectrodes, which can be fabricated out of such films, the obtained results need appropriate considerations. First, because the components of the electrochemical impedance spectroscopy scale non-linearly with size. In addition, the electrochemical activity changes from planar diffusion to spherical diffusion and depending on the available energy states at the electrode-electrolyte interface, the conditions leading to diffusion-limited or kinetic-limited processes can change. The latter is particularly evident in case of semiconductor electrodes, which show a non-negligible bulk resistivity and a space charge region at the electrode-electrolyte interface. However, it appears realistic to expect that better-performing raw-samples at the macroscopic level lead to better-performing MEAs after microfabrication. This is also in agreement with the authors' experimental results of the last decade.

5 Conclusions

This work was aimed at the characterization of the morphological, electrical, electrochemical and optical properties of BDD thin films to be employed in the fabrication of transparent MEAs for *in vitro* cellular biosensing, and in particular to the amperometric applications. More specifically, the characterization was carried out with the purpose of determining an appropriate selection of process parameters to be adopted for the material fabrication. From the reported results, it appears that the temperature plays a role in the substitutional incorporation of boron as dopant in the crystal lattice and that a lower temperature favors the formation of crystal defects or smaller grains in the diamond film, which in turn influence negatively the mobility, thus resulting in an overall higher resistivity. Nevertheless, good results could be achieved as in case of AF93.

Further improvements require the adoption of a different transparent substrate having a thermal expansion coefficient compatible with the one of diamond and at the same time suitable for CVD-process temperature around 750°C, with the hope that an affordable material with such properties can be made available soon.

Acknowledgements GP's work at Ulm University was supported by Erasmus Traineeship programme of the European Union. We are very thankful to Prof. Anna Carbone of Politecnico di Torino, for very stimulating discussions and continuous scientific support. We also wish to express our gratitude to the *Scansetti* Interdepartmental Centre of the University of Torino for the Raman spectroscopy.

6 References

[1] T.C. Granado et al. Progress in transparent diamond microelectrode arrays. Phys. Status Solidi A, 2015, 212, 11, 2445-2453.

[2] D. J. Garrett, et al. Diamond for neural interfacing: A review, Carbon 2016, 102, 437-454.

[3] G. Piret et al. 3D-nanostructured boron-doped diamond for microelectrode array neural interfacing, Biomaterials, 2015, 53, 173-183.

[4] P. Ariano, et al. A diamond-based biosensor for the recording of neuronal activity Biosens Bioelectron, 2009, 24, 2046-2050.

[5] V Maybeck, et al. Boron-Doped Nanocrystalline Diamond Microelectrode Arrays Monitor Cardiac Action Potentials, Advanced healthcare materials 2013, 3, 283-289.

[6] V. Carabelli et al. Nanocrystalline diamond microelectrode arrays fabricated on sapphire technology for high-time resolution of quantal catecholamine secretion from chromaffin cells. Biosensors and Bioelectronics, 2010, 26, 92-98.

[7] Z. Gao et al. Transparent diamond microelectrodes for biochemical application. Diamond and Related Materials, 2010, 19, 1021-1026.

[8] A. Pasquarelli et al. Simultaneous fluorescent and amperometric detection of catecholamine release from neuroendocrine cells with transparent diamond MEAs. Front. Neurosci. 2016. doi: 10.3389/conf.fnins.2016.93.00129

[9] A. Stett et al. Biological application of microelectrode arrays in drug discovery and basic research. Anal Bioanal Chem, 2003, 377, 486–495.

[10] R. Gerwig et al. PEDOT–CNT composite microelectrodes for recording and electrostimulation applications: fabrication, morphology, and electrical properties. Frontiers in Neuroengineering, 2012, 5, 8.

[11] C. Hébert et al. Boosting the electrochemical properties of diamond electrodes using carbon nanotube scaffolds. Carbon, 2014, 71, 27–33.

[12] J. Yao and K.D. Gillis. Quantification of noise sources for amperometric measurement of quantal exocytosis using microelectrodes. Analyst, 2012, 137, 2674.

[13] S.T. Larsen et al. Amperometric Noise at Thin Film Band Electrodes. Analytical chemistry, 2012, 84, 7744-7749.

[14] E. Kohn, K. Janischowsky, W. Ebert. Bias enhanced nucleation of diamond on silicon (100) in a HFCVD system. Diamond and Related Materials, 2003, 12, 336-339.

[15] Z. Gao. Diamond Ultra-small Electrodes for Integration with GaN Electronics, PhD Thesis, Ulm University, 2014.

[16] C. Wild et al. Chemical vapour deposition and characterization of smooth { 100}-faceted diamond films. Diamond and Related Materials, 1993, 2, 158-168.

[17] N. Bozzolo et al. Crystalline quality of highly oriented diamond films grown on 〈100〉 silicon studied by conventional TEM. Diamond and Related Materials, 1997, 6, 41-47.

[18] J. Pernot et al. Hall electron mobility in diamond. Appl. Phys. Lett. 2006, 89, 122111.

[19] P. Gonon et al. Characterization of heavily B-doped polycrystalline diamond films using Raman spectroscopy and electron spin resonance, J. Appl. Phys. 1995, 78, 12, 7059.

[20] W. Gajewski et al. Electronic and optical properties of boron-doped nanocrystalline diamond films. Phys. Rev. B, 2009, 79.

[21] W. P Gomes and D. Vanmaekelbergh. Impedance spectroscopy at semiconductor electrodes: review and recent developments. Electrochemica Acta, 1996, 41, 967-973.

[22] A.J. Bard and L.R. Faulkner. Electrochemical Methods: Fundamentals and Applications, 2nd Edition, Wiley, 2001.

[23] M. E. Orazem, and B.Tribollet: Electrochemical Impedance Spectroscopy, 2nd Edition, Wiley, 2017.

[24] T. Sugino J. Shirafuji. Electrical properties of diamond surfaces, Diamond and Related Materials, 1996, 5, 706-713.

[25] M. Dipalo. Nanocrystalline diamond growth and device applications. PhD Thesis, Ulm University, 2008.

[26] A.C Ferrari and J.Robertson. Origin of the 1150 cm^{-1} Raman mode in nanocrystalline diamond. Phys. Rev. B, 2001, 63, 121405.

[27] M. Bernard et al. About the origin of the low wave number structures of the Raman spectra of heavily boron-doped diamond films. Diamond and Related Materials, 2004, 13, 896-899.

[28] P.W. May et al. Raman and conductivity studies of boron-doped microcrystalline diamond, facetted nanocrystalline diamond and cauliflower diamond films. Diamond and Related Materials 2008, 17, 105-117.

[29] F. Pruvost et al. Characteristics of homoepitaxial heavily boron-doped diamond films from their Raman spectra. Diamond and Related Materials 2009, 9, 295-299.

[30] V. A. Krivchenko et al. Study of polycrystalline boron-doped diamond films by Raman spectroscopy and optical absorption spectroscopy. Technical Physics, 2007, 52, 11, 1471-1474.